Experiment on a confined electrically driven vortex pair

R. Klein[*] and A. Pothérat

Coventry University, Priory Street, Coventry CV1 5FB, United Kingdom

A. Alferenok

Moscow Power Engineering Institute, Institute of Electrical Engineering, Krasnokazarmennaya Street 14, 111250 Moscow, Russia

An experimental study of the transition to turbulence in a confined quasi-two-dimensional magnetohydrodynamic flow is presented. A pair of counterrotating vortice is electrically driven in the center of a thin horizontal liquid metal layer, enclosed in a cylindrical container and subject to a homogeneous vertical magnetic field. When the forcing is increased, the pair is displaced away from the center. Boundary layer separations from the circular wall appear that trigger a sequence of supercritical bifurcations. These are singled out in numerical calculations based on our previously developed shallow water model as well as in the experiment, and these bifurcations are shown to resemble those observed in flows past a cylindrical obstacle. For the highest forcing, the flow then ends up in a turbulent regime where the dissipation increases drastically, which we could relate to a possible transition from a laminar to a turbulent Hartmann boundary layer. Finally we show the first experimental evidence of a transition to three-dimensionality in liquid metal magnetohydrodynamics (MHD) by comparing velocity measurements on either horizontal sides of the layer as we find that columnar vortice wobble for a high enough forcing.

PACS number(s): 47.32.C−, 47.27.Cn, 47.20.Ib

I. INTRODUCTION

We are interested in the transition to turbulence induced by the presence of a wall in quasi-two-dimensional flows. In applications, boundaries are often responsible for the development of turbulence. Their role is, for example, crucial in the dynamics of wings or flying objects where boundary layer separations initiate vortex shedding and subsequent turbulent patterns that, in turn, determine lift and drag forces. The complexity of theses flows makes them difficult to investigate experimentally and very costly to tackle numerically. In this regard, quasi-two-dimensional flows in simpler configurations allow us to easily reproduce some elementary properties of the transitions phenomena that occur in real configurations and to understand the two-dimensional part of their dynamics. This is why a large number of studies have been dedicated to the very generic quasi-two-dimensional separated flow past a circular cylinder (see Refs. [1–3] for a review of numerical work on boundary-generated two-dimensional turbulence). These flows are, to a large extent, determined by how single vortice or vortex pairs interact with walls so it is essential to understand the dynamics of such a reduced system. There has been number of studies around this theme and one can cite two that are closest to our purpose: Ref. [4] demonstrated some elegant visualization of the vortex-wall interaction in liquid metal magnetohydrodynamic (MHD) flows and Ref. [3] recently performed numerical simulations of a forced vortex at the center of a square box. They exhibit a transition to turbulence through a sequence of supercritical bifurcations that leads to a chaotic, then turbulent state, as in the case of the cylinder wake. In

the present work, we aim at reproducing such a boundary induced transition to turbulence experimentally and analyze it, by studying a forced vortex pair confined in a circular domain.

Since a purely two-dimensional flow cannot be achieved experimentally, we wish to put a particular emphasis on the measure of residual three-dimensional effects and their consequences on the quasi-two-dimensional flow. To this end, we study a flow in a thin layer of liquid metal under an externally imposed, transverse magnetic field, as in Ref. [4]. This offers a simple way of reproducing a flow with two-dimensional dynamics. In such a laboratory scale configuration, the feedback action of the flow onto the magnetic field is neglected in the frame of the quasi-static approximation (Ref. [5]). The main effect of the Lorentz force is then to damp velocity variations along the magnetic field lines. If this transverse magnetic field is strong enough, the resulting flow is quasi-two-dimensionality in the sense that physical quantities do not vary across the layer except in the vicinity of the walls that confine it, where so-called Hartmann boundary layers develop because of the nonslip condition (see, for instance, Ref. [6]). Because of this particular flow structure, several small but important laboratory MDH experiments have been built where a layer of liquid metal held between two parallel planes is used to obtain an experimental realisation of quasi-two-dimensional flows. Among them, Ref. [7] has provided an experimental evidence of the two-dimensional inverse energy cascade that characterizes two-dimensional turbulence. References [8,9] experimentally and Ref. [10] numerically have studied the quasi-two-dimensional wake of a circular cylinder and identified the usual regimes found in the hydrodynamic case. In none of these studies, however, was the actual limit of the quasi-two-dimensionality assumption examined, although more general studies have proposed theoretical scenarios for the transition between quasi-two-dimensional and three-dimensional flows

---

*Also at: Applied Mathematics Research Centre, Coventry University.

(see Refs. [11,12]). This question is crucial in order to quantify the relevance of MDH flows in thin layers to two-dimensional flows. We shall therefore address it by calculating the correlations between velocities measured on either side of the fluid layer, just outside of the Hartmann layers as in Ref. [13] where the progressive elongation of a single pulsed vortex subject to a magnetic field was measured. This will allow us to determine whether the observed flow properties are influenced by three-dimensional effects or not.

Our experiment features an horizontal shallow fluid layer enclosed in a cylindrical container in a vertical magnetic field imposed by permanent magnets. A pair of counterrotating vortice is generated by injecting constant electric current through two point electrodes embedded in one of the horizontal, electrically insulating walls as in Refs. [7,4]. The flow characteristics are identified for different values of magnetic field **B** and injected current I. This is done using both numerical simulations from the shallow water model of Ref. [14] and local measurements of electric potential to determine the velocity just outside of the Hartmann layers (e.g., Ref. [15]). We first present numerical calculations and the main flow patterns in Sec. II. In Sec. III A, we describe the experimental setup and the measurement techniques. The experimentally observed flow regimes are presented in Sec. III C and compared to the regimes found numerically in Sec. II. In Sec. III E, we characterize the bifurcations observed at the transition between these flow regimes. Finally we discuss the presence of three-dimensional effects in all observed flow regimes in Secs. III F and III G.

II. THEORY

A. Basic equations

The configuration of interest is that of a liquid metal (viscosity ν, density ρ, and electric conductivity σ) in a cylindrical container of height $a=5$ mm and radius $\widetilde{R}=20$ mm plunged in a steady homogeneous magnetic field **B** directed along the cylinder axis so that $\mathbf{B}=B_z\hat{\mathbf{e}}_z$. The walls of the container are electrically insulating and the flow is driven by connecting the two poles of a current generator to two metallic electrodes (diameter $d_e=1$ mm) embedded in the bottom plate at locations $(0,d,0)$ and $(0,-d,0)$ (see Fig. 6), where the origin is taken at the center of the bottom plate of the container. It is known from Ref. [11] that when the magnetic field is strong enough, the flow is invariant along the magnetic field lines, except near the wall orthogonal to the field where Hartmann layers with an exponential velocity profile develop. The Lorentz force then acts indirectly on the flow by shaping those layers, which in turn exert a linear friction on the resulting quasi-two-dimensional flow. The flow is now well described by two-dimensional motion equations obtained by averaging the full three-dimensional equations along the magnetic field lines, as in Ref. [11]. This model will thereafter be referred to as SM82. In the present cylindrical geometry, the high curvature of the streamlines, however, induces some strong inertial effects that disturb this simplified picture: Ref. [14] has indeed shown that strong rotation triggers a local Ekman pumping that leads to impor-

tant velocities along the magnetic field lines. Although quasi-two-dimensionality may still be achieved in the sense that the horizontal velocities in the core flow are still invariant along the magnetic field lines, these secondary flows lead to a significant redistribution of the flow's momentum that can drastically change the global dissipation. Reference [14] has further proposed a refinement of the SM82 model, denoted PSM, that accounts locally for these secondary flows through higher order nonlinear terms, and that we shall apply to our problem. In nondimensional variables, the PSM equations that govern the evolution of quantities averaged spatially along $\hat{\mathbf{e}}_z$ between the two Hartmann walls located at $z=0$ and $z=a$ yield

$$\mathbf{\nabla}_\perp \cdot \mathbf{u}_\perp = 0, \tag{1}$$

$$(\partial_t + \mathbf{u}_\perp \cdot \mathbf{\nabla}_\perp)\mathbf{u}_\perp + \mathbf{\nabla}_\perp p - \frac{N}{\mathrm{Ha}^2}\nabla_\perp^2 \mathbf{u}_\perp$$

$$= -2\frac{N}{\mathrm{Ha}}\mathbf{u}_\perp + \frac{2}{\mathrm{Ha}\,N}\left(\frac{7}{36}\mathcal{D}_{\mathbf{u}_\perp} + \frac{1}{8}\partial_t\right)\mathbf{u}_\perp \cdot \mathbf{\nabla}_\perp \mathbf{u}_\perp + \mathbf{f}, \tag{2}$$

where the operator $\mathcal{D}_{\mathbf{u}_\perp}$ is defined as

$$\mathcal{D}_{\mathbf{u}_\perp}:\mathbf{F} \mapsto \mathcal{D}_{\mathbf{u}_\perp}\mathbf{F} = (\mathbf{u}_\perp \cdot \mathbf{\nabla}_\perp)\mathbf{F} + (\mathbf{F} \cdot \mathbf{\nabla}_\perp)\mathbf{u}_\perp. \tag{3}$$

Quantities averaged along $\hat{\mathbf{e}}_z$ are by definition dependent only on x and y. The corresponding Nabla operator $\mathbf{\nabla}_\perp$ is two-dimensional and carries the subscript $(\ )_\perp$. Similarly, the same subscript on a vector indicates components perpendicular to the magnetic field only. All quantities have been further normalized using the dimensional quantities U_0 and a as reference velocity and distance. Furthermore, the superscript on observed quantities such as velocities, velocity fluctuations, and distances, thereafter presented in the experimental part Sec. III denotes a dimensional quantity (e.g., $R=\widetilde{R}/a$ as the dimensionless counterpart of $\widetilde{R}$). The square of the Hartmann number $\mathrm{Ha}=aB_z\sqrt{\sigma/(\rho\nu)}$ and the interaction parameter $N=\sigma B_z^2 a/(\rho U_0)$ represent the ratio of the Lorentz forces to viscous and inertial forces, respectively, so both are required to be larger than unity for the PSM model to be valid.

Out of the two additional terms that appear in the right-hand side of Eq. (2), the first one is linear and results from the friction induced by the Hartmann layer on the two-dimensional flow. The associated dimensional Hartmann damping time $t_H=(1/2)(a^2/\nu)(1/\mathrm{Ha})$ strongly decreases with B_z, indicating the nature of the magnetohydrodynamic (MHD) effect: when the magnetic field increases, the Hartmann layer becomes thinner thus inducing a stronger friction on the flow. The other additional terms are nonlinear and result from the redistribution of momentum due to local Ekman pumping. The model also provides the expression of the dimensionless velocity u_z along the field lines just outside the Hartmann layer (for a mathematically rigorous definition of this concept, see Refs. [16,17]):

TABLE I. Nondimensional parameters and related time step in cases calculated numerically.

regime	I		II				III	IV							
Re^0	216	2164	4328	6494	7576	8116	8658	9740	10822	11904	12986	15152	17316	21644	28138
Re^M	89.8	846	1567	2250	2580	2740	2898	3245	3573	3894	4188	4768	5281	6122	7174
R_δ^{num}	0.5	4.9	9.1	13.1	15	15.9	16.9	18.9	20.8	22.6	24.4	27.7	30.7	25.6	41.7
N_v	137.2	13.7	6.9	4.6	3.9	3.7	3.4	3.0	2.7	2.5	2.3	2.0	1.7	1.4	1.1
Δt	0.05	0.01	0.005	0.01/3	0.01/3	0.01/3	0.0025	0.0025	0.002	0.002	0.002	0.002	0.002	0.001	0.001

$$u_z(z=0) = -\frac{5}{6}\frac{a^2}{\widetilde{R}^2}\frac{1}{\text{Ha}\,N_v}\boldsymbol{\nabla}_\perp \cdot [(\mathbf{u}_\perp \cdot \boldsymbol{\nabla}_\perp)\mathbf{u}_\perp], \qquad (4)$$

where $N_v = N\widetilde{R}/a \geq 1$ is the interaction parameter based on the horizontal scale. The ratio $u_z/\|\mathbf{u}_\perp\|$ gives a good indication as to where Ekman pumping is important. $u_z > 0$ ($u_z < 0$) indicates that fluid is expelled from (injected in) the Hartmann layers to (from) the core flow. Some detailed accounts of this effect are presented in Refs. [14,18,19].

The forcing $\mathbf{f}$ results from the interaction of the electric current injected at the electrodes with the external magnetic field, which, by virtue of the Hartmann layer theory is equivalent to imposing a vorticity along $\hat{\mathbf{e}}_z$, proportional to the injected current. Following Refs. [7,14], the forcing imposed on the flow by an electric current I injected through an electrode of diameter d_e, with the center located at $\mathbf{r}_e$ expresses dimensionally as

$$\mathbf{f}(\mathbf{r}) = \frac{\Gamma}{t_H}\frac{\mathcal{H}\left(\|\mathbf{r}-\mathbf{r}_e\| - \dfrac{d_e}{2}\right)}{\|\mathbf{r}-\mathbf{r}_e\|}\hat{\mathbf{e}}_\theta^e, \qquad (5)$$

where $\Gamma = I/(2\pi\sqrt{\sigma\rho\nu})$ is the total circulation induced by the current injection at one electrode and $\mathcal{H}$ is the Heaviside step function. $\hat{\mathbf{e}}_\theta^e$ denotes the azimuthal direction with respect to the center of the electrode. Since the nondimensional forcing $\mathbf{f}$ that appears in Eq. (2) is induced by the two electrodes with opposite polarities, respectively, located at $\mathbf{r}_e^+ = d\hat{\mathbf{e}}_y$ and $\mathbf{r}_e^- = -d\hat{\mathbf{e}}_y$, it can be written in nondimensional form as

$$\mathbf{f}(\mathbf{r}) = \frac{\widetilde{R}}{a}\frac{N}{\text{Ha}}\left(\frac{\mathcal{H}\left(\|\mathbf{r}-\mathbf{r}_e^+\| - \dfrac{d_e}{2}\right)}{\|\mathbf{r}-\mathbf{r}_e^+\|}\hat{\mathbf{e}}_\theta^+ - \frac{\mathcal{H}\left(\|\mathbf{r}-\mathbf{r}_e^-\| - \dfrac{d_e}{2}\right)}{\|\mathbf{r}-\mathbf{r}_e^-\|}\hat{\mathbf{e}}_\theta^-\right),$$
$$(6)$$

where $\hat{\mathbf{e}}_\theta^+$ ($\hat{\mathbf{e}}_\theta^-$) again points in the azimuthal direction with respect to the electrode located at $\mathbf{r}_e^+$ ($\mathbf{r}_e^-$). This suggests $U_0 = 2\Gamma/d$ as a reference velocity *a priori* with the corresponding Reynolds number $\text{Re}^0 = U_0\widetilde{R}/\nu$ and underlines the fact that the ratio of two-dimensional inertial effects to the Lorentz force is measured by $(\widetilde{R}/a)(N/\text{Ha})$, rather than the interaction parameter N. Similarly, since U_0 is derived from the forcing only, and ignores all types of dissipation present in the flow [viscous, Hartmann layer friction, effect of three-dimensional (3D) recirculations], it is clearly larger than the true flow velocity, albeit of the same order of magnitude. A more realistic Reynolds number Re^M based on the maximum velocity along $\hat{\mathbf{e}}_x$ and therefore calculated *a posteriori* is therefore given alongside Re^0 in Table I that can be used as an *a priori* control parameter.

Finally, a nonslip boundary condition is applied at the impermeable wall located at $\|\mathbf{r}\| = R$. Note that Eq. (2) implies that this wall is electrically insulating.

Before proceeding with the numerical resolution of the PSM equation presented in this section, it is worth recalling that this model is a shallow water approximation [such as those widely used in geophysical flows (see Ref. [20])], obtained by integration of the full Navier-Stokes equations along the magnetic field. This integration is performed by approximating the velocity profile in the z direction at order 2 for the small parameters Ha^{-1} and N_ν^{-1}. At this order, the Hartmann layer is assumed laminar and the three-dimensional velocity field $\mathbf{u}_{\text{Ha}}(x,y,z,t)$ within the Hartmann layer expresses as

$$\mathbf{u}_{\text{Ha}}(x,y,z,t) = \mathbf{u}^{\text{core}}(x,y,t)f(z), \qquad (7)$$

where $f(z)$ represents both the two-dimensional flow in the core with the velocity field $\mathbf{u}^{\text{core}}(x,y,t)$ and the classical exponential velocity profile in the laminar Hartmann layer. In the PSM model, however, this profile is modified to account for inertial effects of order N_ν^{-1} (see Ref. [6]), while the horizontal velocity outside these layers is invariant in the z direction. Since $f(z)$ is obtained from assumptions in the limit of small Ha^{-1} and N_ν^{-1}, the model is free from artificial modelling but also implies that it becomes imprecise when either of the parameters Ha^{-1} or N_ν^{-1} becomes of order 1. Reference [21] has shown that for $N < 1$, the secondary flows due to local Ekman pumping are overestimated (note that values of N_ν for our simulations are given in Table I).

The validity of the model of Ref. [14] is further affected depending on whether the Hartmann layer is laminar or turbulent. From the form of Eq. (7), three important cases can be distinguished.

(a) If the velocity field $\mathbf{u}^{\text{core}}(x,y,t)$ becomes turbulent while $f(z)$ remains unaffected, the flow is in a quasi-two-dimensional turbulent state, but still with a laminar Hartmann layer and the PSM model from Ref. [14] remains valid.

(b) If the Hartmann layer becomes turbulent, the function $f(z)$ takes a different form although the core flow outside the layer may still be two-dimensional, as observed by Ref. [22]. In this case the PSM model breaks down as it cannot account for a turbulent Hartmann layer profile nor for the transition between a laminar and a turbulent Hartmann layer. This transition happens at the critical Reynolds number $R_\delta = \text{Re}^M/\text{Ha}$

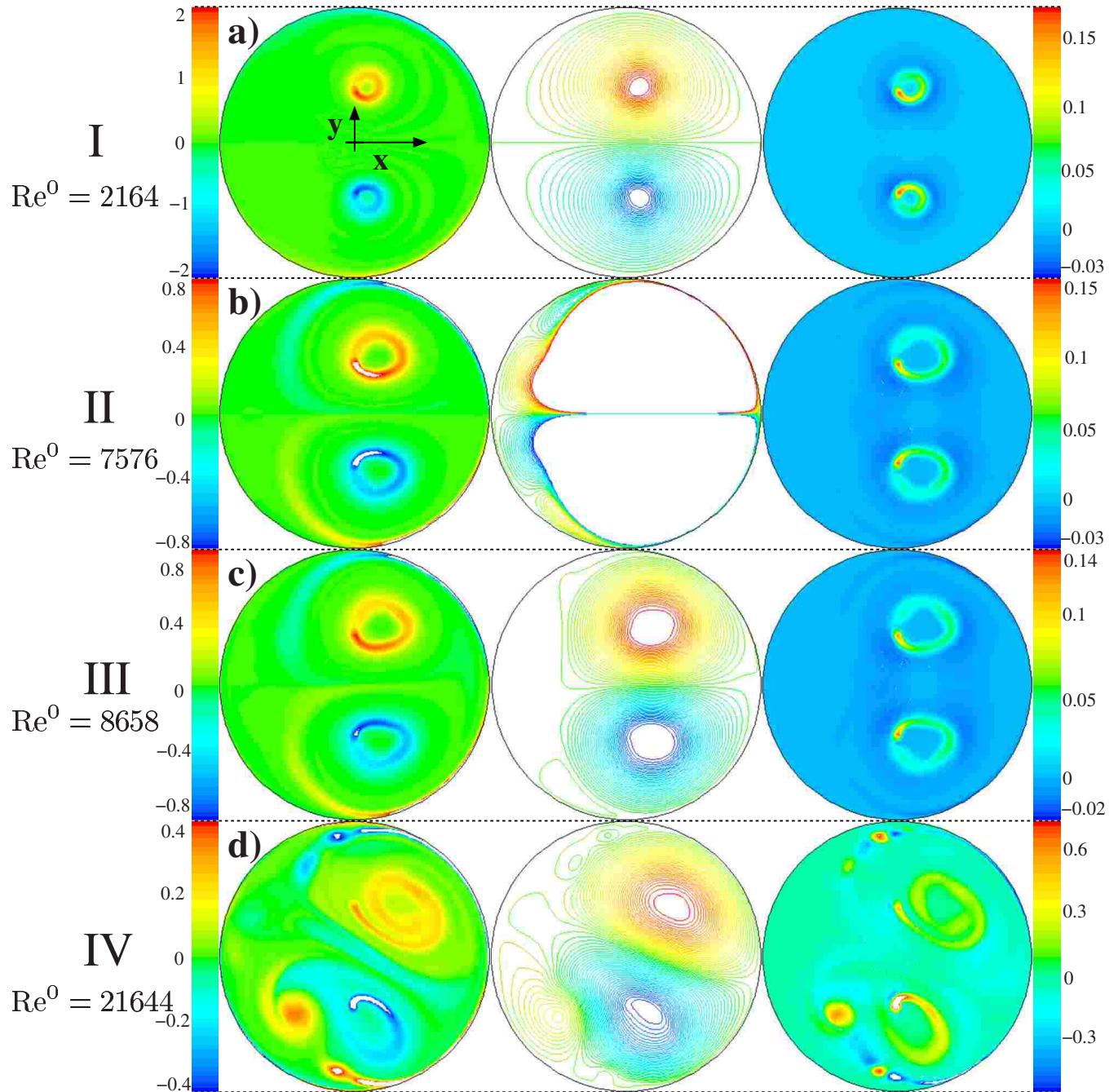FIG. 1. (Color online) Snapshots of equilibrium and quasi-equilibrium states in all flow regimes for Ha=43 obtained from numerical simulations. Contours of vorticity normalized by U_0/a (left column), streamlines (center column), contours of vertical velocity as given by Eq. (4), normalized by U_0 (right column). (a) Regime I, (b) regime II, (c) regime III, (d) regime IV.

in the case of a channel flow (see Ref. [23]). In the present simulations, however, R_δ^{num} remains an oder of magnitude below this critical value (see Table I).

(c) If the flow is in a state of full three-dimensional turbulence, the velocity field may not take the form of Eq. (7) anymore. In spite of the above limitations, the PSM model is better suited to our goal of finding the main flow patterns than three-dimensional direct numerical simulations for several distinct reasons: on the top of its simplicity and natural precision at high Ha and N_ν, PSM removes the necessity of meshing the very thin Hartmann layers and also eliminates

the coupling between velocity and electric potential that is inherent to the 3D MHD equations. The resolution of these coupled equations demands special care indeed, in order to be accurately resolved (see Refs. [24,25]).

B. Numerical model

We shall now solve the system (2) numerically, in order to visualise the different flow states when the electric current is increased. Velocity profiles recorded along diameter $y=0$ will then be compared to the measurements from the experi-

ment in Sec. III in order to help identify the regimes found experimentally, as no global flow visualization is possible in our setup. The comparison can, however, only remain qualitative as wall roughness present in the experiment is not modeled in the numerical simulation. The latter is expected to stabilize the flow and to shift the transitions between quasi-two-dimensional flow regimes identified in this section further. Since the initial problem has been reduced to a two-dimensional one thanks to the PSM model, we are now left with the task of solving the unsteady equations (2) on a disk of radius R. To this end, we use the numerical method and mesh described and tested in Ref. [19], where a numerically similar problem to ours is considered, but with a different forcing. Also, compared to theirs, our numerical system now uses a third instead of a second order spatial discretization, which slightly improves precision, especially on the unstructured part of the mesh. All computations are performed for Ha=43 with the fluid initially at rest and with the injected current I (hence Re^0) set to a constant value. The calculation runs until the total energy of the flow is stable over a time much longer than t_H or than all remaining oscillations. Averaged quantities reported thereafter are then computed over a time interval of several times t_H. Table I summarizes the different cases we have simulated.

C. General aspect of the flow

When the forcing is increased from $I=0$, the final flow state goes through a sequence of bifurcations that can be seen from the contours of vorticity and streamlines represented on Fig. 1. We shall now describe these globally, whereas local quantities such as velocity profiles are reported together with experimental results in Sec. III.

At very low forcing, i.e., at low Re^0, the flow essentially consists of two steady counterrotating vortice, antisymmetric about the $\hat{e}_x$ axis and centred slightly to the right of the electrode axis [Fig. 1(a)]. The distance between the axis of their centers and that of the electrodes results from the balance between their mutual influence that tends to imprint a motion toward $x>0$, and the influence of the circular wall. Each of these vortice presents a sharp vorticity maximum located away from the vortex centre that corresponds to a free shear layer in the shape of a ring. This first steady regime will be denoted "I" thereafter and the corresponding Re^0 are displayed in Table I.

For slightly higher values of Re^0, the flow remains steady but the boundary layers located along the cylinder wall or side layers separate in two symmetric locations behind the vortice so a small counterrotating recirculation appears behind each of the initial vortice [Fig. 1(b)]. These two antisymmetric recirculation regions are analogous to those in duct flows past a cylindrical obstacle with an homogeneous magnetic field oriented along the cylinder axis, as studied by Ref. [10]. Unlike these, however, those from the present problem remain apart from each other as the main flow reattaches to the cylinder wall. The length of the recirculation region along the wall, however, increases with Re^0. By analogy with Ref. [10], we will call this second steady flow regime "regime II" (see Table I).
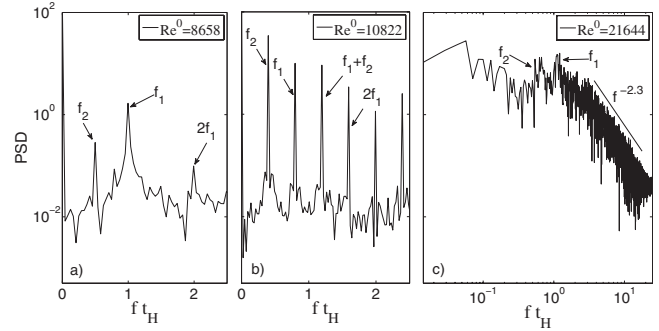

FIG. 2. Power density spectra obtained from $u(0,t)$ for Ha=43. Energy and frequencies are normalized by $U_0^2/2$ and t_H^{-1}, respectively. (a) Re^0=8658, regime III. (b) Re^0=10 822, regime IV. (c) Re^0=21 644, regime IV. Note that for Re^0=8658 the flow is nearly in regime IV, however, the amplitude of the corresponding oscillation with frequency f_2 remains small.

For higher Re^0 a new regime (regime III, see Table I) appears where the separated boundary layers at the back of the vortice destabilize. Vortice form there and grow along the layer until they are released in the stream between the two electrodes, resulting in the appearance of a low frequency f_1 in the oscillations of the velocity field see [Figs. 1(c) and 2(a)]. This shedding process is reminiscent of that in the Von Kàrmàn street behind a cylindrical obstacle (see Refs. [1,10]), but differs from it in two ways: first, at the forcing for which this phenomenon first appears, vortice are released almost simultaneously and not in turn. This synchronization is, however, lost at slightly higher forcing. Second, two very weak additional vortice are released along the centerline in the direction $x<0$. The frequency spectrum of $|u_x^2(0,t) +u_y^2(0,t)|$ that characterizes this regime exhibits strong peaks for the fundamental frequency f_1 of vortex shedding as well as for the higher harmonic $2f_1$ [Fig. 2(a)].

A further flow regime, called regime IV (see Table I) is found when a lower base frequency f_2 appears in the frequency spectrum [see Fig. 2(b)]. In this regime, the central vorticity rings are strongly disrupted and exhibit both short and long wave instabilities. Also, vortice that shed in the direction $x<0$ become stronger so the global picture is that of a strongly chaotic flow. Interestingly, Ref. [10] also pointed out the appearance of a lower frequency in the regime he calls IV, where the Von Kàrmàn street is disrupted by vortice generated due to boundary layer separation at the duct side walls. The periodic Von Kàrmàn street regime they find, however, spans a much larger interval of Re^0. The reason is that in our case, the vortex shedding process is immediately disturbed by the reinjection of shed vortice in the main stream, whereas the flow around the cylinder has to reach much higher velocities for shed vortice to produce some boundary layer separation at the duct walls.

Further regime changes at higher forcing are much more difficult to detect as the flow becomes fully turbulent. At Re^0=21644, the spectrum exhibits the $|u_x^2(0,t)+u_y^2(0,t)|$ $\sim f^{-2.3}$ power law in the mid range [see Fig. 2(c)]. A spatial energy spectrum can be deduced from these frequency spectra by defining the wave number sequence as $k=f|u(0,t)|$. Since at this location, the flow is dominated by a strong jet in
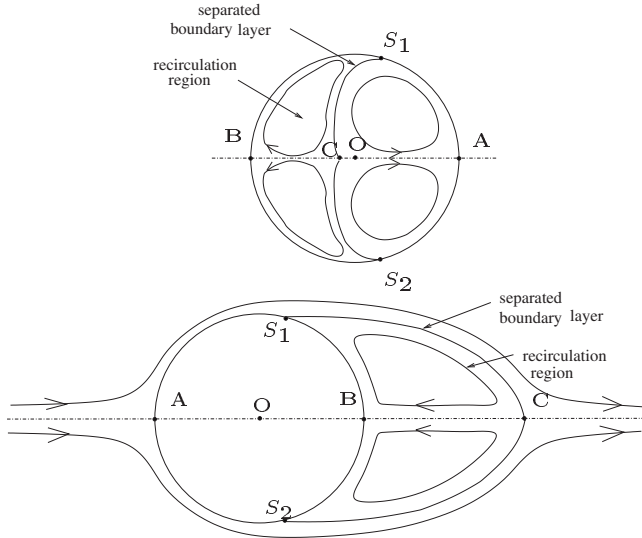
FIG. 3. Steady flows and flows with separations within (top) and outside (bottom) a cylinder. A, B, and C are stagnation points, S_1 and S_2 are separation points.

the direction $\hat{\mathbf{e}}_x$, $k_x \sim f|\langle u(0,t)\rangle|$, where $\langle u(0,t)\rangle$ is the time average from $u(0,t)$. This implies that $|u_x^2(0,t) + u_y^2(0,t)| \sim k_x^{-2.3}$. For $\mathrm{Re}^0 = 21\,644$ and $\mathrm{Re}^0 = 28\,138$ (Table I) which are the highest in our numerical simulations, however, one can expect the secondary flows to be slightly overestimated as N_ν comes close to unity (see Ref. [21]).

D. Similarities with the flow around a cylinder

To further investigate the similarity between the present flow and the duct flow past a cylinder under axial magnetic field studied by [10], we define the base pressure coefficient $C'_{pb} = (p_A - p_C)/[\rho(\tilde{u}_x^M)^2]$ where $\tilde{u}_x^M$ is a dimensional quantity and denotes the maximum velocity of $\tilde{u}_x$ along the diameter $\tilde{y} = 0$ (p_A as well as p_C refer to the pressure at stagnation points A and C, respectively, as displayed in Fig. 3). Its variation as a function of $\mathrm{Re}^M = \tilde{u}_x^M \tilde{R}/\nu$ (see Table I for values of Re^M) and Re for fixed Ha is shown in Fig. 4(a) for a
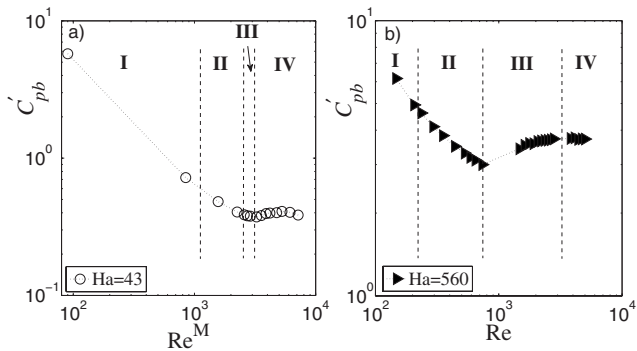

FIG. 4. Base pressure coefficients C'_{pb} in flow regimes I, II, III, and IV obtained from numerical simulations. (a) C'_{pb} vs Re^M for the flow within a cylinder for Ha=43. (b) C'_{pb} vs Re for a flow past a cylinder for Ha=560 (see Ref. [10]). Re is built on average velocity at the duct inlet.
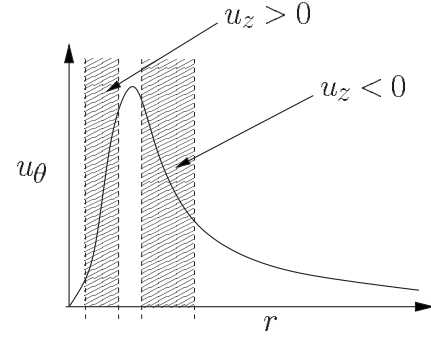

FIG. 5. Typical profile of an electrically driven vortex (see, for instance, Refs. [4,14]). A strong flow from the Hartmann layers to the core appears in vortex core, while a strong reverse flow takes place in the high velocity region just outside the core

flow within the cylinder and for a flow past the cylinder in Fig. 4(b) (found by Ref. [10]), respectively. For the latter, the Reynolds number Re is built on average velocity at the duct inlet. Although only high Hartmann results are available from Ref. [10], the evolution of C'_{pb} is similar between both problems throughout regimes I to III [see Figs. 4(a) and 4(b)]. In particular, C'_{pb} decreases in the steady regime and increases in the unsteady regime. Evolutions of C'_{pb} for flows that are well in regime III and thereafter in regime IV differ but this might be due to the effect of three-dimensional recirculations which become dominant since N_v approaches unity in the cases calculated here. These recirculations are known to significantly increase the dissipation in concave parallel layers (see Refs. [14,19]) and can therefore be expected to influence C'_{pb} strongly. They are, however, suppressed at such high values of N_v such as those from Ref. [10].

E. Effect of the Ekman recirculations

The third column from Fig. 1 shows the contours of $u_z(x,y)$ calculated from Eq. (4). This equation implies that this quantity is larger where horizontal velocity gradients are more important as strong fluid sources and sinks appear in the core flow. The associated horizontal transport of angular momentum can drastically increase the viscous dissipation, in particular where boundary layers are involved, as shown in Ref. [19].

A further effect is that vortice are surrounded by regions where the fluid plunges into the Hartman layers, as also shown by the three-dimensional numerical simulations of Ref. [26] in the non-MHD case. This can be understood by considering an axisymmetric clockwise vortex, centered at the origin, with typical profile shown on Fig. 5. Then, Eq. (4) implies that $u_z(r) \sim 1/r\partial_r u_\theta^2$. Near the vortex center, the velocity must be zero so $u_\theta \sim r^\alpha$ with $\alpha > 0$ and $u_z(r) \sim 2\alpha r^{2\alpha-1}$. This means that a strong Ekman pumping is present there with $u_z > 0$. Further out, the velocity is high but decreases as $u_\theta \sim r^\alpha$, with $\alpha < 0$ this time, so a surrounding region with strong vertical velocities toward the Hartmann layers must exist just outside the vortex core.
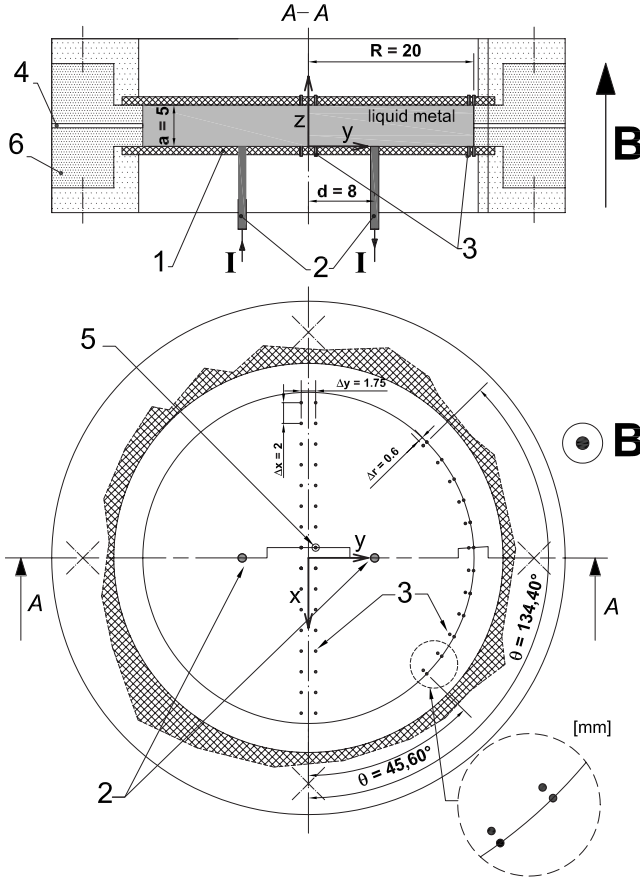
FIG. 6. Experimental apparatus. Top: cross section of the cylindrical container, bottom: top view of the bottom plate. (1) Electric board, (2) electric current injection electrodes (diameter $d_e = 1$ mm), (3) electric potential probes, (4) inlet and outlet to fill cavity with GaInSn, (5) reference probe for electric potential measurements, (6) plexiglas hollow cylinder. $\Delta \tilde{x} = 2.5$ mm, $\Delta \tilde{y} = 1.75$ mm, and $\Delta \tilde{r} = 0.6$ mm are the distances between the potential probes.

III. EXPERIMENT

A. Experimental setup and measurement techniques

The main experimental apparatus (Fig. 6) is made of a closed cylindrical container with radius $\tilde{R} = 20$ mm and height $a = 5$ mm, where all walls are electrically insulating. The cavity is hermetically filled with GaInSn, a metal alloy liquid at room temperature (electric conductivity $\sigma = 2.3 \times 10^6$ S/m, density $\rho = 6440$ kg/m^3, viscosity $\nu = 4 \times 10^{-7}$ m^2/s). The top and bottom plates of thickness 1.5 mm are made of fiber-reinforced epoxy FR4, which is a standard material for electronic boards.

Once filled, the apparatus is centered inside the gap between two sets of identical permanent magnets (surface 120×100 mm). Magnetic fields of $B_z = 0.09$ T, $B_z = 0.12$ T, $B_z = 0.19$ T, and $B_z = 0.24$ T with maximum inhomogeneity of 10% along $\hat{\mathbf{e}}_y$, 4% along $\hat{\mathbf{e}}_x$, and 1% along $\hat{\mathbf{e}}_z$ over the fluid domain, are achieved by adjusting the gap width.

The flow is forced by injecting constant electric current I through two copper electrodes (diameter $d_e = 1$ mm) fitted flush to the bottom wall at $(0, d, 0)$ and $(0, -d, 0)$ and with $d = 8$ mm. Both electrodes are connected to a regulated DC

TABLE II. Characteristic Hartmann friction time t_H and Hartmann number Ha.

B [T]	0.09	0.12	0.19	0.24
$t_H = \dfrac{a^2}{2\nu} \dfrac{1}{\mathrm{Ha}}$ [s]	3.3	1.75	1.1	0.85
$\mathrm{Ha} = aB \sqrt{\dfrac{\sigma}{\rho\nu}}$	13.5	18	28.5	36

power supply, providing electric currents in the range $I \in [0 - 20A]$ with a maximum ripple 0.5×10^{-3} A.

Electric potential ϕ is measured locally thanks to two symmetric sets of 56 potential probes (diameter $\phi d_{pr} = 0.25$ mm) embedded in the top and bottom wall, respectively, at locations sketched on Fig. 6. The two sets are aligned exactly opposite each other along the $\hat{\mathbf{e}}_z$ axis. The measured signals are typically of the order of 10 μV and must therefore be amplified by a high precision, low-noise system. We use a 112 multichannel single ended amplifier-system with gain 111 and integrated 24 bit A/D converter for every channel, that measures each electric potential with respect to one electric potential probe (reference probe), located near the box center (see Fig. 6). All signals are simultaneously recorded at a sampling rate of 128 Hz, for which the peak to peak noise is about 2 μV.

As, e.g., noticed by Refs. [15,7], the electric current density in the core flow $\|\mathbf{j}^{\mathrm{core}}\|$ is small in quasi-two-dimensional and even weakly three-dimensional flows so Ohm's law in the core flow can be approximated by $-\nabla \phi^{\mathrm{core}} + \mathbf{u}^{\mathrm{core}} \times \mathbf{B} \simeq 0$, to a precision of the order of $\frac{\|\mathbf{j}^{\mathrm{core}}\|}{\sigma}$. Since the variation of electric potential across the boundary layer is $O(\delta/a)$, with $\delta = \frac{a}{\mathrm{Ha}}$ as the Hartmann layer thickness, the electric potential field in the core is nearly that measured at the Hartmann wall, to this same precision. Combining these two arguments leads to $-\nabla \phi_{\mathrm{wall}} + \mathbf{u}^{\mathrm{core}} \times \mathbf{B} \lesssim O(\max|\frac{\delta}{a}, \frac{\|\mathbf{j}^{\mathrm{core}}\|}{\|\mathbf{u}^{\mathrm{core}} \times \mathbf{B}\|}|)$. As long as $\frac{\delta}{a} \ll 1$ and $\frac{\|\mathbf{j}^{\mathrm{core}}\|}{\|\mathbf{u}^{\mathrm{core}} \times \mathbf{B}\|} \ll 1$, the velocity just outside the Hartmann layer can be deduced from probes embedded in the wall and, respectively, distant by $\Delta \tilde{x}$ and $\Delta \tilde{y}$ from one another by Fig. 6:

$$\tilde{u}_x = -\frac{1}{B_z} \left(\frac{\tilde{\phi}_{\mathrm{wall}}(\tilde{x}, \tilde{y} + \Delta \tilde{y}) - \tilde{\phi}_{\mathrm{wall}}(\tilde{x}, \tilde{y})}{\Delta \tilde{y}} \right),$$

$$\tilde{u}_y = \frac{1}{B_z} \left(\frac{\tilde{\phi}_{\mathrm{wall}}(\tilde{x} + \Delta \tilde{x}, \tilde{y}) - \tilde{\phi}_{\mathrm{wall}}(\tilde{x}, \tilde{y})}{\Delta \tilde{x}} \right). \quad (8)$$

In order to take advantage of Eq. (8), the probes have been placed so as to obtain profiles of velocities $\tilde{u}_x$ and $\tilde{u}_y$ along the diameter $\tilde{y} = 0$ (Fig. 6). Velocity profiles $\tilde{u}_\theta(\tilde{r}, \theta, t)$ near the side walls at $\tilde{r} = 19.7$ mm for $\theta \in [45.6°, 134.4°]$ (see Fig. 6) are measured in the same way, however using $\Delta \tilde{r} = 0.6$ mm as radial spacing between probes. Finally it is important to notice that even if the Hartmann layer becomes turbulent, its thickness δ remains very thin (see Ref. [27]) so the assumption $\frac{\delta}{a} \ll 1$ is still valid. Furthermore, the core flow above a turbulent Hartmann layer also remain two-

dimensional, provided the turn-over time $l_\perp/u$ of turbulent vortice, of size $l_\perp$ and spinning velocity u, remains large compared to the time of two-dimensionalization $\frac{\rho}{\sigma B^2}\frac{a^2}{l_\perp^2}$ (see Refs. [11,22]). This suggests that Eq. (8) remains valid, even when the Hartmann layer becomes turbulent. Finally, in order for three-dimensionality to spoil the validity of Eq. (8), the current in the core would have to be $O(\mathbf{u}^{\mathrm{core}}\times\mathbf{B})$. This only occurs in strongly three-dimensional flows so the method presented here also applies to weakly three-dimensional flows, albeit with a larger error than in quasi-two-dimensional flows.

Electric potentials, measured on potential probes aligned exactly opposite each other along the $\hat{\mathbf{e}}_z$ axis, allow us to derive the velocity correlations between points located just outside the Hartmann layer on either wall. A velocity correlation coefficient lower then one indicates that the flow is three-dimensional in the sense that the velocity varies along the magnetic field lines outside the Hartmann layer.

B. Experimental procedure

Starting at $I=0A$, the electric current is first increased in steps of $0.1A$ up to the maximum value of $I=10A$. If a bifurcation is found at critical electric current I_c, the step size is reduced to $0.01A$ within the range $I_c\pm0.05A$. Once $I_c+0.05A$ is reached, a possible hysteresis around I_c is sought by decreasing the current in the same steps. The electric current I is expressed under nondimensional form through the Reynolds number Re^0 that measures the forcing (see Sec. II A). For each forcing we wait several times the Hartmann friction time t_H until the flow is fully developed and start then recording time dependent electric potentials over at least $10t_H$ (Table II). Quantities averaged in time in the established flow regime are denoted $\langle\cdots\rangle$ thereafter.

This procedure is repeated for four different values of magnetic field strength B_z, which correspond to nondimensional Hartmann numbers Ha presented in Table II. Ha as well as Re^0 are then the two control parameters in this experiment. Thus, critical values $\mathrm{Re}^0_{\mathrm{III}}$, $\mathrm{Re}^0_{\mathrm{IV}}$, $\mathrm{Re}^0_{\mathrm{V}}$, and Re^0_{3D} mentioned thereafter, are in fact functions of the Hartmann number as shown in Fig. 7.

C. Flow regimes identified from velocity profiles

For weak forcing, such that $\mathrm{Re}^0<\mathrm{Re}^0_{\mathrm{II}}$, the flow is steady and the corresponding profile of u_x [marked by "I" in Fig. 8(a)] along the diameter $y=0$ is almost symmetric about $x=0$, with $u_x>0$ everywhere. In this regime, the point of maximum velocity u_x^M is, however, located at $x^M>0$, x^M being small and increasing with Re^0 [Fig. 9(a)]. Velocities $u_\theta(r=0.985R,\theta,t)$, measured near the cylinder wall, are anticlockwise oriented and almost azimuthal, without any sign reversal (Fig. 10). In the numerical simulations (Sec. II C) this type of profile is typical from regime I [Fig. 11(a)], and the location of the maximum velocity u_x^M along the diameter $y=0$ corresponds to the position of the initial vortex pair.

For $\mathrm{Re}^0\gtrsim\mathrm{Re}^0_{\mathrm{II}}$, the flow changes to a second steady state (regime II), where the velocity profile $u_\theta(r=0.985R,\theta,t)$ first

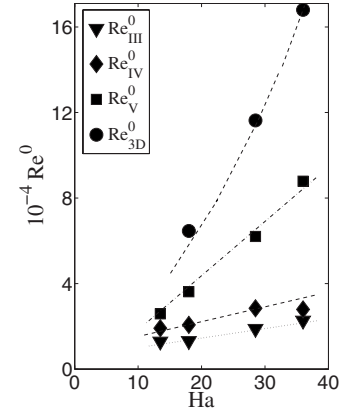FIG. 7. Critical Reynolds numbers vs Hartmann number. $\mathrm{Re}^0_{\mathrm{III}}$: transition from the steady flow regime to the periodic flow regime. $\mathrm{Re}^0_{\mathrm{IV}}$: transition from the periodic flow regime to the flow regime with two base frequencies. $\mathrm{Re}^0_{\mathrm{V}}$: transition to the flow regime where the profile of u_x almost becomes symmetric again. Re^0_{3D}: transition to three-dimensionality (see Sec. III F).

exhibits a change of sign at angle $\theta_{s'}$ (Fig. 10), that corresponds to the separated boundary layer found in Sec. II C. When the forcing is further increased, the flow still remains steady and $\theta_{s'}$ is displaced along the wall in clockwise direction [Fig. 9(c)]. This displacement also coincides with the increase of x^M, which indicates that it is a consequence of the displacement of the initial vortex pair in the $x>0$ direction.
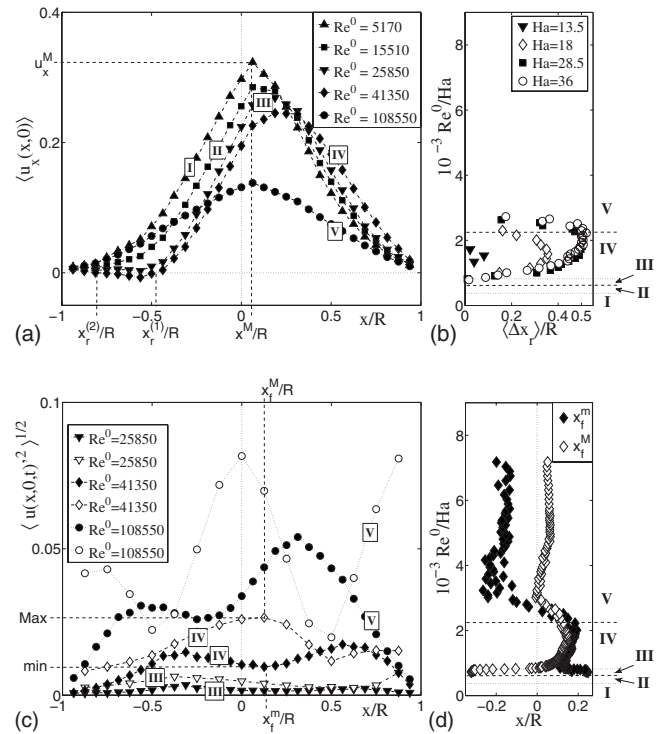

FIG. 8. Time averaged quantities. (a) Velocity profiles $\langle u_x(x,0)\rangle$ for Ha=36. (b) Width of recirculating region $\langle\Delta x_r\rangle=\langle x_r^{(1)}-x_r^{(2)}\rangle$ vs $\mathrm{Re}^0/\mathrm{Ha}$. (c) r.m.s. of velocity fluctuations $u'(x,0,t)$ along the diameter $y=0$ for Ha=36. Black markers: $\langle u_x'(x,0,t)^2\rangle^{1/2}$, white markers: $\langle u_y'(x,0,t)^2\rangle^{1/2}$. (d) x_f^m and x_f^M vs $\mathrm{Re}^0/\mathrm{Ha}$ for Ha=36. The corresponding flow regimes are indicated as I, II, III, IV, and V.
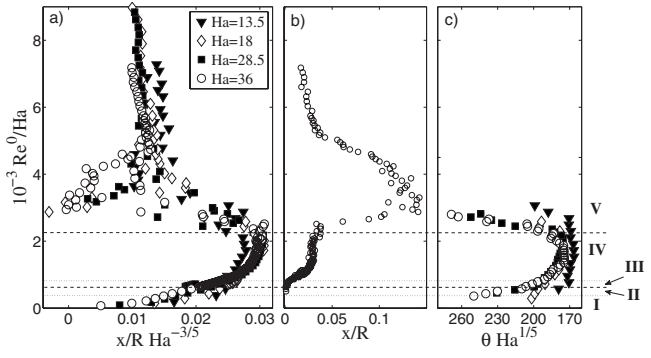
FIG. 9. (a) $\langle x^M \rangle$ vs Re^0/Ha. (b) Standard deviation $\sigma(x^M)$ vs Re^0/Ha for $Ha=36$. (c) $\langle \theta_{s'} \rangle$ vs Re^0/Ha.
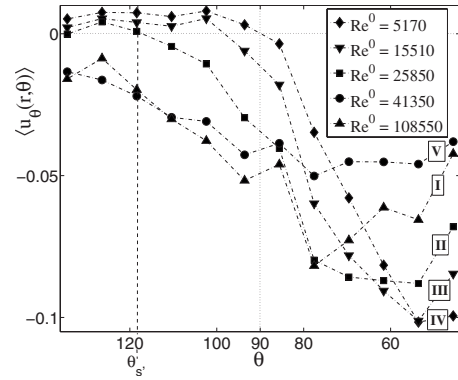

FIG. 10. Time averaged velocity profiles $\langle u_\theta(r=0.985R, \theta) \rangle$ along the circular box side wall for $Ha=36$. Note that the precise determination of $\theta_{s'}$ is limited by the number of measurement points along the side wall and a low signal to noise ratio.

The zone of positive azimuthal velocity for $\theta > \theta_{s'}$ in Fig. 10 therefore characterizes the antisymmetric counterrotating recirculation regions that appear behind each of the two initial vortice because of the separated boundary layer (see Sec. II C).

The unsteady flow regime sets in at $Re^0=Re_{III}^0$ ["III" in Fig. 8(a)]. It results in a periodic oscillation in $\phi(x,y,t)$ and is characterized by strong peaks with base frequency f_1 and further harmonics $2f_1$ and $3f_1$ in the frequency spectrum. Corresponding spectra, recorded from measurements on the top plate at $x=-0.4375R$ and $y=-0.04375R$ are shown on Fig. 12(a) (power spectra taken from potential measurements at other locations yield qualitatively similar results). Accordingly, x^M and $\theta_{s'}$ are time-dependent and when the forcing is intensified, $\langle x^M \rangle$ and the standard deviation $\sigma(x^M) = \langle [x^M(x,0,t)-\langle x_M(x,0)\rangle]^2 \rangle^{1/2}$ increase. Also, $\langle \theta_{s'} \rangle$ is displaced along the circular wall in the $\theta < 0$ direction [see Fig. 9(c)]. The good qualitative agreement between numerical and experimental mean velocity profiles, as well as the r.m.s. of velocity fluctuations $\mathbf{u}'(x,0,t)$, with $u_x(x,0,t)' = u_x(x,0,t)-\langle u_x(x,0) \rangle$ and $u_y(x,0,t)' = u_y(x,0,t)-\langle u_y(x,0) \rangle$, proves that these measurements characterize the vortex shedding regime found in numerical simulations [Figs. 11(a) and 11(b) and Figs. 8(a) and 8(c), respectively]. This also explains the presence of maxima at $x<0$ in the profiles III of $\langle u_x'(x,0,t)^2 \rangle^{1/2}$ and $\langle u_y'(x,0,t)^2 \rangle^{1/2}$ plotted along the diameter $y=0$, as they correspond to the location where the shed vortice impact onto the centerline [see Figs. 11(b) and 8(c)].

For $Re^0=Re_{IV}^0$, a second base oscillation f_2, with $f_2 < f_1$, appears in the frequency spectrum of $\phi(x,y,t)$. The spectrum

is then seen to be extended as further frequency peaks occur for Re^0 slightly higher than Re_{IV}^0 [Fig. 12(b)] and exihibts a $A \sim f^{-2.3}$ power low for $Re^0 \gg Re_{IV}^0$ [Fig. 12(c)]. This equates to regime IV identified in the numerical simulations as here again, the time averaged profiles of velocity as well as r.m.s. profiles of velocity fluctuations, obtained numerically and experimentally are in good qualitative agreement [see Figs. 11(a) and 11(b) and Figs. 8(a) and 8(c), respectively]. In this regime, a clear maximum in the profiles of $\langle u_y'(x,0,t)^2 \rangle^{1/2}$ appears in the region $x>0$ at x_f^M [Fig. 8(c)], roughly at the location x^M where $u_x=u_x^M$ [Fig. 8(a)]. It is due to the two initial vortice starting to oscillate and periodically crossing the centerline $y=0$. Furthermore, the vorticity carried by shed vortice induces a flow of negative mean velocity in the $x<0$ region on the centerline and the width of this region $\langle \Delta x_r \rangle = \langle x_r^{(1)}-x_r^{(2)} \rangle$ increases with the forcing as the associated return flow intensifies [see Figs. 8(a) and 8(b)]. Once sucked into the stream between the two oscillating vortice located at $x>0$, these shed vortice are strongly squeezed and stretched along $\hat{\mathbf{e}}_x$. This points to the minimum in the profile $\langle u_x'(x,0,t)^2 \rangle^{1/2}$ at x_f^m [see Fig. 8(c)]. Since this stretching is directly induced by the two initial vortice, the evolution of x_f^m follows that of x_f^M with increasing forcing, until these two points clearly separate, which marks the end of regime IV.

A last change of flow regime has been detected at $Re^0 = Re_V^0$, where all quantities are brutally altered. $\langle \Delta x_r \rangle$ drastically shrinks [Fig. 8(b)] and negative velocity components
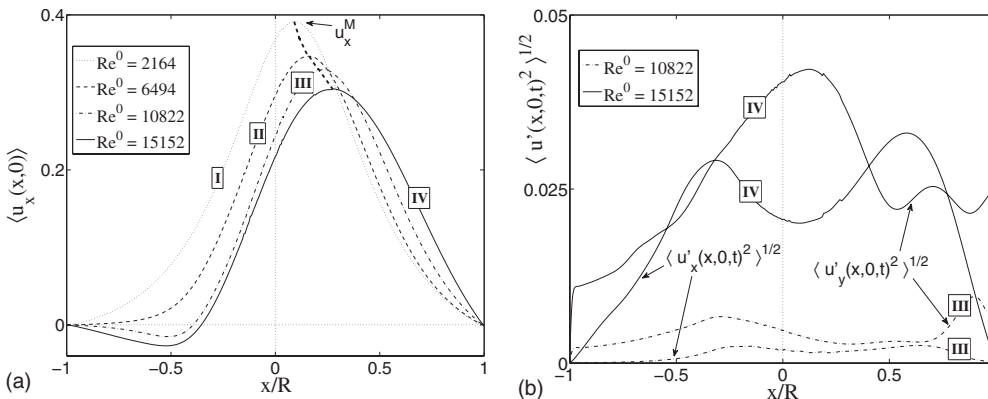

FIG. 11. Time averaged quantities obtained from numerical simulations for $Ha=43$. (a) Velocity profiles $\langle u_x(x,0) \rangle$. (The thick dashed line indicates the shift of the vortex pair toward $x>0$ with increasing Re^0.) (b) $\langle u_x'(x,0,t)^2 \rangle^{1/2}$ and $\langle u_y'(x,0,t)^2 \rangle^{1/2}$ along the diameter $y=0$.
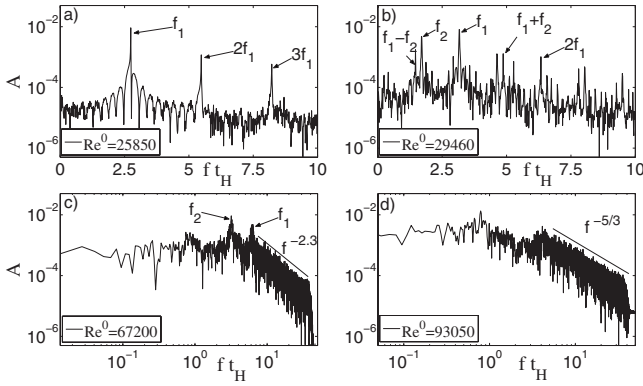
FIG. 12. FFT of recorded time-dependent signal $\phi(x=-0.4375R, y=-0.04375R, t)$ for Ha=36. (a) Periodic flow (regime III). (b) Two base frequency flow (regime IV). (c) Chaotic or turbulent flow in flow regime IV. (d) Chaotic or turbulent flow in flow regime V. Oscillation amplitudes A and frequencies f_i are normalized by $B_z U_0 a$ and the Hartmann friction time t_H^{-1}, respectively.
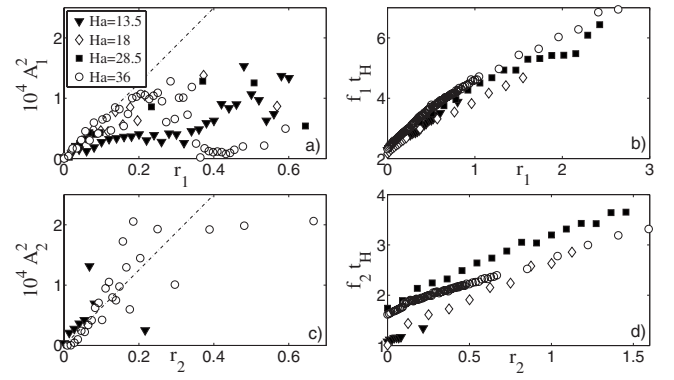

FIG. 13. Nature of bifurcations. (a) Square of the amplitude A_1 of mode 1 vs r_1. (b) Frequency f_1 of mode 1 vs r_1. (c) Square of the amplitude A_2 of mode 2 vs r_2. (d) Frequency f_2 of mode 2 vs r_2. Oscillation amplitudes A_i and frequencies f_i are normalized by $B_z U_0 a$ and the Hartmann friction time t_H^{-1}, respectively.

vanish completely along the diameter $y=0$, resulting in a profile of $\langle u_x \rangle$ that is almost symmetric about $x=0$ [Fig. 8(a)]. Accordingly, the average $\langle x_M \rangle$ rapidly drops to the vicinity of $x=0$ at first, increases again and then slightly decreases for higher forcing. Also, the averaged point of sign reversal along the circular wall $\langle \theta_{s'} \rangle$ is displaced in anticlockwise direction, thus following the displacement of $\langle x^M \rangle$. For $\text{Re}^0 \gg \text{Re}_V^0$, very strong velocity fluctuations make the detection of $\theta_{s'}$ in the profile $u_\theta(r=0.985R, \theta, t)$ impossible.

Figures 12(c) and 12(d) show that the amplitude of all measured frequencies raises significantly above that from previous regimes. According to Ref. [3] this indicates a transition to a spectrum with a broad continuous component, thus implying that the flow in regime V is turbulent. This regime is also characterised by the emergence of a new peak frequency much lower than f_2, as well as a $A \sim f^{-5/3}$ inertial range.

D. Scaling laws based on R_h

The critical values $\text{Re}_{III}^0, \text{Re}_{IV}^0, \text{Re}_V^0$ that correspond to the transitions between the regimes identified in the previous section are shown on Fig. 7. With the exception of the case Ha=13.5, all critical Reynolds numbers scale as Ha, indicating that they may be governed by a single parameter $R_h = \text{Re}^0/\text{Ha}$. In order to further check this property, all Re^0 dependent quantities have been plotted against R_h instead of Re^0 [see Figs. 8(b), 9(a), and 9(c)]. It clearly appears that any set of curve describing a topological quantity ($\langle x^M \rangle$, $\langle \theta_{s'} \rangle$, $\langle \Delta x_r \rangle$) can be merged into a single one, provided they are, respectively, scaled as

$$\frac{\langle x^M \rangle}{\text{Ha}^{3/5}} \sim f(\text{Re}^0/\text{Ha}), \quad \langle \theta_{s'} \rangle \text{Ha}^{1/5} \sim g(\text{Re}^0/\text{Ha}),$$

$$\langle \Delta x_r \rangle \sim h(\text{Re}^0/\text{Ha}). \tag{9}$$

The fact that the lower values of Ha (Ha=13.5 and less noticeably Ha=18) match these scalings imperfectly certainly

indicates that these are valid in the limit of large Ha and breakdown at lower Ha, where three-dimensional effects are present, as will be seen in Sec. III F. The relevance of R_h as governing parameter in quasi-two-dimensional MHD flows has been pointed out long ago (see Refs. [4,7]) in flows dominated by Hartmann friction. It is, however, remarkable that this parameter keeps its relevance in the present case where strong three-dimensional recirculations due to some local Ekman pumping are present. This certainly indicates that the extra global dissipation induced by these remains small compared to the Hartmann friction and that they essentially alter the local shape of individual vortice. Velocity profiles across any of them (which are not available in the experiment) may indeed not follow an universal law expressed in terms of R_h only, as in the case of Sommeria's isolated vortice in Ref. [4], where local recirculations affect the vortex core only.

E. Nature of the bifurcations at $\text{Re}^0 = \text{Re}_{III}^0$ and $\text{Re}^0 = \text{Re}_{IV}^0$

We have analyzed the nature of the bifurcation at $\text{Re}^0 = \text{Re}_{III}^0$ by plotting the amplitude A_1 of mode 1 with fundamental frequency f_1 versus the critical parameter $r_1 = \text{Re}^0/\text{Re}_{III}^0 - 1$ on Fig. 13(a). It is found to follow a square root function. This, together with the fact that no hysteresis at transition to regime III was observed, indicates a supercritical bifurcation. The corresponding coefficients from the Landau theory (see Refs. [28,29]) can be extracted by interpolating $A_1(r_1)$ as

$$|A_1| \simeq \sqrt{\frac{2k_1 r_1}{l_1}} = \sqrt{\frac{2\sigma_1}{l_1}}, \tag{10}$$

where σ_1 is the exponential growth rate, $k_1 = \text{const}$ and l_1 measures the nonlinear saturation in the perturbation growth. For $0 < r_1 < 0.15$, the interpolation of $A_1(r_1)$ with a square root function yields $k_1/l_1 \simeq 3 \times 10^{-4}$ for all values of Ha, but Ha=13.5 [see Fig. 13(a)]. Here again, the case Ha=13.5 departs from the asymptotic curve and exhibits stronger saturation. Also, the related base frequency f_1 increases linearly for small r_1 as a function of Re^0 and seems to saturate for

higher r_1 as the flow approaches regime IV [Fig. 13(b)]. Furthermore, the frequency f_1 at the onset of regime III increases monotonically with Ha. The second bifurcation at $Re^0 = Re_{IV}^0$ results in a spectrum with two base frequencies f_1 and f_2 and subsequent linear combinations [Fig. 12(b)] of the form $m_1 f_1 + m_2 f_2$ with $(m_1, m_2) \in \{-2, -1, 0, 1, 2\}^2$ as in Refs. [30,3]. As for mode 1, the fundamental frequency f_2 of mode 2 increases linearly with the critical parameter $r_2 = Re^0 / Re_{IV}^0 - 1$, but the slope seems to depend weakly on Ha [Fig. 13(d)]. No saturation was detected for $0 < r_2 < 1.5$ but it may well occur for higher forcing. As $A_1(r_1)$, $A_2(r_2)$ follows a square root function without any measurable hysteresis. An interpolation of $A_2(r_2)$ for $0 < r_1 < 0.15$ yields also $k_2 / l_2 \simeq 3 \times 10^{-4}$ [Fig. 13(c)], and one can conclude to the supercritical nature of the bifurcation to regime IV as well.

F. Measure of three-dimensionality

The three-dimensionality of the flow is measured by the correlation between values of quantity $V_T(t)$ and $V_B(t)$, taken at the same location (x, y) at top and bottom plate, respectively. Two different types of correlation functions are used:

$$C_1 = \frac{\sum_{i=0}^{n} V_B(t) V_T(t)}{\sqrt{\sum_{i=0}^{n} V_B^2(t) \sum_{i=0}^{n} V_T^2(t)}} \quad \text{and} \quad C_2 = \frac{\sum_{i=0}^{n} V_B(t) V_T(t)}{\sum_{i=0}^{n} V_B^2(t)},$$

(11)

where n is the number of samples over which C_1 and C_2 are calculated. C_1 quantifies how much phase and frequency are correlated, regardless of signal amplitudes. C_2 is the more usual correlation function, that incorporates the signal amplitude. Correlations based on the velocity component $u_x(x, 0, t)$ are denoted C_2 thereafter.

Correlations built on velocity fluctuations $u_x'(x, 0, t) = u_x(x, 0, t) - \langle u_x(x, 0) \rangle$ are denoted by C_1' and C_2'. At this point, it should be stressed that the correlation factor can be influenced by the presence of $\simeq 2 \ \mu V$ peak to peak noise, especially in regimes I and II where the signals are weak, and the ratio $r_{S/N}$ between the amplitude of the signal and that of the noise, respectively, is small. For example, $r_{S/N} \simeq 5$ for $Re^0 = 5170$ and $Ha = 36$. This induces an error of $\simeq 10\%$ in the correlation factor C_2. This deviation from $C_2 \simeq 1$, however, quickly decreases for higher values of Re^0, as $r_{S/N}$ becomes much larger. Consequently, this error is already as small as $\simeq 0.25\%$ and hence negligibile when the flow changes to regime III.

The variations of C_i and C_i' with Re^0 are depicted on Figs. 14(a), 14(c), and 14(d) for several values of Ha. When Ha $= 36$ and Ha $= 28.5$, the velocity correlation C_2 is nearly unity for all investigated regimes and one can conclude that the flow is very close to quasi-two-dimensionality. For Ha $= 18$, C_2 seems to be slightly below unity even for very high $r_{S/N}$'s, indicating some small three-dimensionality. For Ha $= 13.5$, this effect is more substantial, and one sees that three-dimensionality is always present. This certainly explains why the case Ha $= 13.5$ departs from all the others in the scaling

laws found in the previous section. The picture turns out to be a little more refined when inspecting the correlations based on the velocity fluctuations [Figs. 14(c) and 14(d)]. Both C_1' and C_2' are weak near the onset of unsteadiness as fluctuations and hence the $r_{S/N}$ is small. They eventually increase to a value of about unity and remain almost constant for $Re^0 \lesssim Re_{3D}^0$. Here again, the small deviation is due to the presence of noise. However, correlations close to unity at all locations (x, y) along the centerline [Fig. 14(b)] indicate quasi-two-dimensionality in this flow regime. Furthermore, the fact that $C_1' \simeq C_2'$ tells us that the velocity fluctuations are strongly correlated in phase, frequency and amplitude.

This behavior changes drastically at the critical value $Re^0 = Re_{3D}^0$ (values for Re_{3D}^0 are given on Fig. 7). Both C_1' and C_2' linearly decrease for $Re^0 > Re_{3D}^0$ while C_2 remains almost constant [see Figs. 14(a), 14(c), and 14(d)]. This indicates the presence of three-dimensional vortice even though the mean flow remains quasi-two-dimensional. It can be seen from the profiles of velocity correlations in Fig. 14(b) that these three-dimensional structures are mostly located in the region $x > 0$ where vortice are strongly accelerated by the mean flow. Furthermore, since C_2' declines more strongly than C_1', one can conclude to a smaller amplitude of the velocity fluctuations on the top plate. The decrease in C_2' also tells us that the flow in these structures is not only slower on the top plate than on the bottom plate, but also shifted in phase and frequency. In other words, the quasi-two-dimensional columnar vortice start wobbling.

It is noteworthy that for Ha ≥ 28.5, Re_{3D}^0 is much larger than Re_V^0 so three-dimensionality appears well into turbulent flow regime V, whereas regimes I, II, III, IV are strictly quasi-two-dimensional. Also, Re_{3D}^0 scales approximately as $Ha^{8/5}$, except for the lower values of Ha, Ha $= 18$ and 13.5. In these cases, the region of influence of the noise is extended as signals are weaker, so one can not tell whether the plateau $C_1' \simeq C_2' \simeq 1$ is reached for $Re^0 < Re_{3D}^0$. On the other hand, for these low values of Ha, higher values of $Re^0 / Ha^{8/5}$ could be reached and a new regime appears at $Re^0 = Re_p^0$, where both C_1' and C_2' stop decreasing and stay constant for all $Re^0 > Re_p^0$ [see Fig. 14(c) and 14(d)]. This behavior can be due to residual viscous friction and local Ekman pumping at the scale of each vortex, that transports momentum along $\hat{\mathbf{e}}_z$. Furthermore, since the electric current is injected at the bottom plate, the motion near the top plate is mostly be induced by the motion near the bottom so they cannot be totally uncorrelated.

G. Hartmann layer friction

Our experimental setup does not allow for measurements made directly within the Hartmann layer nor for a global measurement of the dissipation as obtained in the experiment of Ref. [23]. We can, however, obtain a rough measure of the fraction of the injected energy that is passed on to the quasi-two-dimensional flow in the jet along the diameter $y = 0$ by monitoring the evolution of $\alpha_{2D} = (\tilde{u}_x^M / U_0)^2$ vs R_δ (we recall that $\tilde{u}_x^M$ is the maximum velocity in the time averaged velocity profile [see Fig. 8(a)]). In this regard α_{2D} is analogous to the friction factor F defined in Ref. [23] in the sense that it
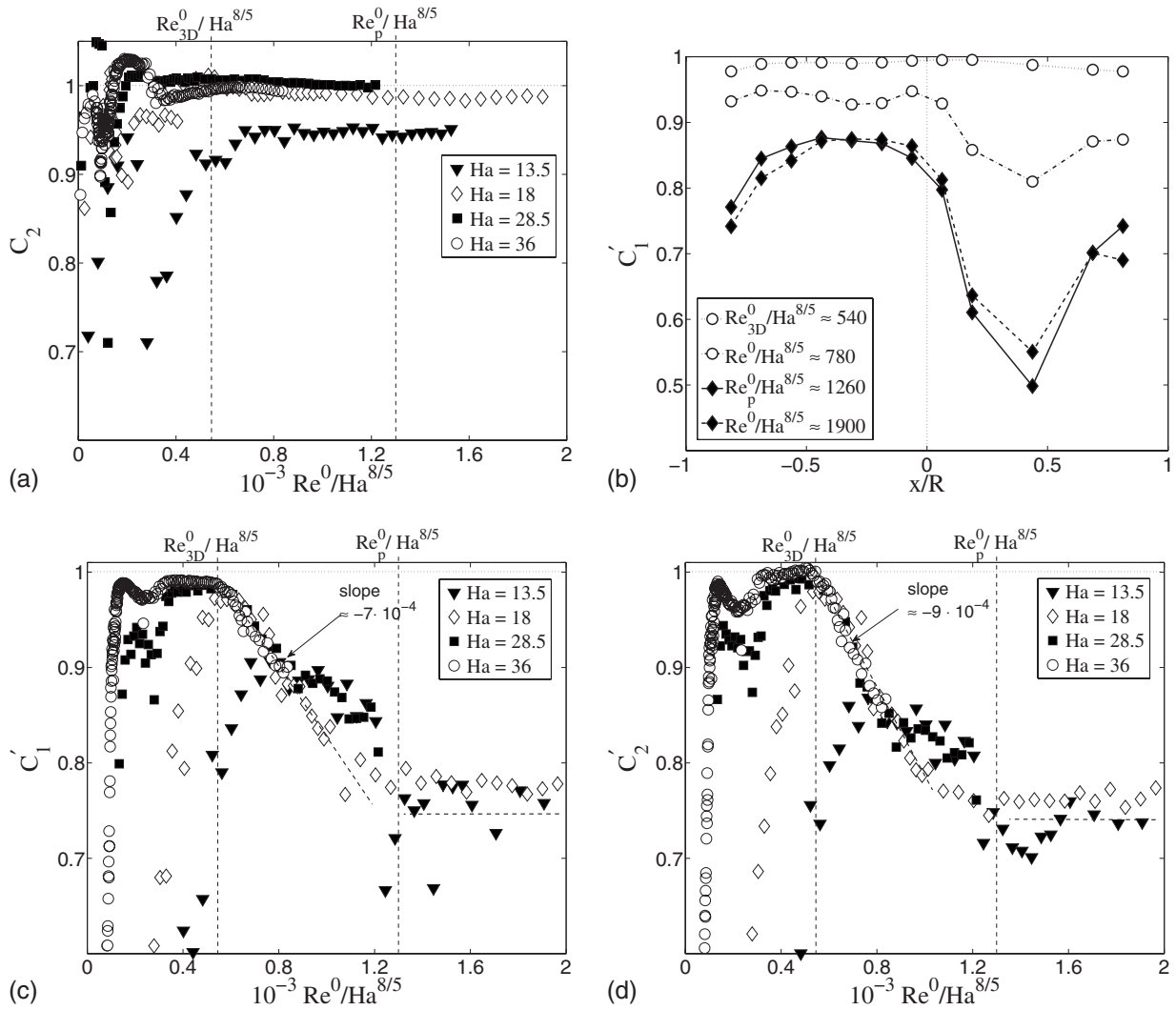
FIG. 14. Correlations averaged along the diameter $y=0$ for $x \in [-0.8125R, 0.8125R]$ and vs $\mathrm{Re}^0/\mathrm{Ha}^{8/5}$. (a) C_2. (b) Profile of C_1' along the diameter $y=0$. (c) C_1'. (d) C_2'.

represents a ratio between a velocity built on the forcing and a measured velocity (here $\tilde{u}_x^M$). Also, as in Ref. [23] R_δ represents the Reynolds number based on the Hartmann layer thickness as well as on a velocity derived from measurements of electric potentials, and it controls the transition from a laminar to a turbulent Hartmann layer. Reference [23], however, measure their voltage across the whole channel, which gives them an average flow velocity whereas our measurement corresponds to the maximum velocity in the driving jet along $\hat{\mathbf{e}}_x$. In this sense both R_δ's reflect the same physics, except that ours is local while that in Ref. [23] is global.

The energy not transmitted to $(\tilde{u}_x^M)^2$ is either dissipated or transmitted to the three-dimensional part of the flow so a change in the Hartmann friction should reflect on the evolution of α_{2D}.

Figure 15 presents the evolution of α_{2D} vs R_δ. For Ha $=28.5$ and 36, and R_δ lower than the critical value for the transition to regime V ($R_\delta^V \simeq 120$), α_{2D} decreases almost linearly with R_δ. Since the flow is close to quasi-two-dimensionality in this regime (see Figs. 7 and 14), this es-

sentially reflects joule dissipation in the Hartmann layers (or Hartmann friction). For $R_\delta > R_\delta^V$, α_{2D} suddenly drops (see Fig. 15). Here, the flow is still quite close to quasi-two-dimensionality as $\mathrm{Re}^0 < \mathrm{Re}^{3D}$ (see Fig. 14). This suggests that the extra dissipation might come from a brutal change in
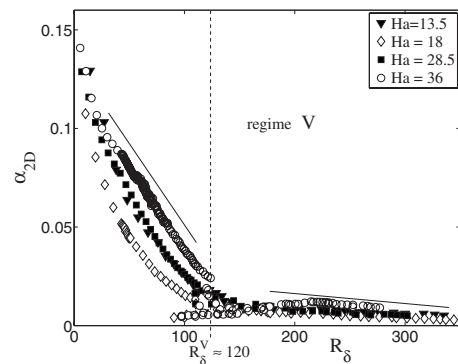

FIG. 15. $\alpha_{2D}=(\tilde{u}_x^M/U_0)^2$ vs $R_\delta=\tilde{u}_x^M(\delta_{\mathrm{lam}}/\nu)$ for all Ha. Note that $\tilde{u}_x^M$ and therefore R_δ drops strongly at the onset of regime V for Ha$=18$, 28.5, and 36, and increases again within regime V.

the Hartmann layer friction, triggered by a transition from a laminar to a turbulent Hartmann layer. It may certainly be objected that the critical value $R_\delta \simeq 120$ is well below $R_\delta \simeq 380$ found in recent experimental (see Ref. [23]) and numerical (see Ref. [22]) studies on rectangular duct flows. This, however, might be related to the fact that our forcing mechanism is not the same as in Ref. [23] and therefore triggers a different flow. While the flow in the experiment of Ref. [23] is expected to be steady when the Hartmann layer destabilizes, the flow in the present work, although still close to quasi-two-dimensionality, is already strongly turbulent, because of instabilities initialised in the side layers. The presence of a complex turbulent flow in the vicinity of the measurement points introduces uncontrolled perturbations that are absent in the idealized configurations cited above. On the top of this several other factors such as wall roughness (see Ref. [23]) as well as a large number of potential probes on the Hartmann walls could generate additional disturbances and also lead to a destabilization of the Hartmann layer for lower R_δ than in Ref. [23].

For $R_\delta \gg R_\delta^V$, α_{2D} decreases almost linearly with R_δ again for all Ha but with a gentler slope than at low R_δ (see Fig. 15). For these values of R_δ, $Re^0 > Re^0_{3D}$ so three-dimensional perturbations are also present that generate some additional Joule dissipation in the core flow on the top of the dissipation in the turbulent Hartmann layer.

IV. CONCLUSION

We have performed an experiment where a vortex pair confined by a circular wall was created by injecting electric current into a thin layer of liquid metal perpendicular to an homogeneous magnetic field. Such a flow is known to be almost quasi-two-dimensional as physical quantities hardly vary along the field lines, except in the fine Hartmann boundary layers at the top and bottom plates (see Refs. [11,14]). This allowed us to perform numerical simulations based on the shallow water model of Ref. [14], that accounts for moderate Ekman pumping locally. In the experiment, electric potential measurements have been used to determine part of the two-dimensional velocity field. Both methods were cross checked in order to identify the different regimes spanned by the system when the electric current is increased. It was shown that the system undergoes a transition to turbulence through a sequence of supercritical bifurcations that are very similar to those observed in the wake of a circular cylinder (see Ref. [10]). First, two recirculating bubbles appear behind the initial vortex pair as the boundary layer on the circular wall separates in two symmetric points (regime II). Secondly the separated boundary layer becomes unstable and

vortice shed and are sucked in the jet between these initial vortice (regime III). Unlike a cylinder wake where shed vortice are released downstream, vortice are reinjected into the main flow making it more unstable, so the flow quickly becomes chaotic as the forcing is increased (regime IV). Further insight into the analogy between these two systems could be obtained by investigating their properties as dynamical systems. Such a task was undertaken by Ref. [3] who has identified a clear scenario for the transition to turbulence of a single vortex in a square box from two-dimensional direct numerical simulation. It is worth mentioning that the frequency spectra found in the present study strongly resembles that found in theirs.

At higher injected electric current, we have identified another transition in the quasi-two-dimensional flow patterns where the velocity profile along the center diameter becomes almost symmetric (regime V). This regime was beyond the validity range of our numerical model so the exact flow patterns remain unclear. We noticed, however, a drastic drop at $Re_0 = Re_0^V$ exactly, in the slope of $\alpha_{2D} = (\bar{u}_x^M / U_0)^2$ vs R_δ, the Reynolds number based on the thickness of the Hartmann layer, that points to a likely transition to turbulence in this region.

Finally, we have checked the two-dimensionality of the system by calculating correlations between velocities measured on the same magnetic field line, on the top and bottom walls enclosing the fluid layer. It turns out that for Ha ≥ 28.5 the flow is very close to quasi-two-dimensionality in all investigated regimes as correlations are nearly unity. When these correlations are based on the velocity fluctuations only, a sudden decrease appears well into regime V which we could show is due to columnar vortice not only having different rotation rates at the top and bottom plates, but also wobbling. This provides the first evidence of a transition between quasi-two-dimensional and three-dimensional turbulence in forced liquid metal MHD flows. Since this transition occurs well into regime V for Ha ≥ 28.5, this also allows us to be certain that regime I, II, III, and IV are strictly quasi-two-dimensional and reflect two-dimensional dynamics. Clearly though, further experiments in a larger box are needed, where a higher number of measurement points as well as a measurements in the bulk of the flow should help determine the mechanisms of this transition to three-dimensionality.

[1] M. Zdravkovich, *Flow Around Circular Cylinders* (Oxford University Press, Oxford, 1997), Vol. 1.

[2] M. Zdravkovich, *Flow Around Circular Cylinders* (Oxford University Press, Oxford, 2003), Vol. 2.

[3] D. Molenaar, H. J. H. Clercx, and G. J. F. van Heijst, Phys. Rev. Lett. **95**, 104503 (2005).

[4] J. Sommeria, J. Fluid Mech. **189**, 553 (1988).

[5] P. Roberts, *Introduction to Magnetohydrodynamics* (Longs-

mans, London, 1967).

[6] R. Moreau, *Magnetohydrodynamics* (Kluwer Academic Publisher, Dordrecht, 1990).

[7] J. Sommeria, J. Fluid Mech. **170**, 139 (1986).

[8] O. V. Andreev and Y. B. Kolesnikov, in *3rd International Conference on Transfer Phenomena in Magnetohydrodynamics and Electroconducting Flows, Aussois, France*, pp. 205–210 (1997).

[9] M. Frank, L. Barleon, and U. Müller, Phys. Fluids **13**, 2287 (2001).

[10] V. Dousset and A. Pothérat, Phys. Fluids **20**, 017104, (2008).

[11] J. Sommeria and R. Moreau, J. Fluid Mech. **118**, 507 (1982).

[12] P. A. Davidson, J. Fluid Mech. **336**, 123 (1997).

[13] B. Screenivasan and T. Alboussiere, J. Fluid Mech. **464**, 287 (2002).

[14] A. Pothérat, J. Sommeria, and R. Moreau, J. Fluid Mech. **424**, 75 (2000).

[15] A. Kljukin and A. Thess, Exp. Fluids **25**, 298 (1998).

[16] S. Kaplun, Z. Angew. Math. Phys. **9**, 111 (1954).

[17] A. Pothérat, J. Sommeria, and R. Moreau, Phys. Fluids **14**, 403 (2002).

[18] P. Dellar, J. Fluid Mech. **515**, 197 (2004).

[19] A. Pothérat, J. Sommeria, and R. Moreau, J. Fluid Mech. **534**, 115 (2005).

[20] J. Pedlosky, *Geophysical Fluid Dynamics* (Springer Verlag, Berlin, 1987).

[21] P. A. Davidson and A. Pothérat, Eur. J. Mech. B/Fluids **21**, 541 (2002).

[22] D. S. Krasnov, E. Zienicke, O. Zikanov, T. Boeck, and A. Thess, J. Fluid Mech. **504**, 183 (2004).

[23] P. Moresco and T. Alboussiere, J. Fluid Mech. **504**, 167 (2004).

[24] L. Leboucher, J. Comput. Phys. **150**, 181 (1999).

[25] M. Ni, R. Munipalli, P. Huang, N. B. Morley, and M. A. Abdou, J. Comput. Phys. **227**, 205 (2007).

[26] M. P. Satin, A. W. Cense, R. Verzicco, H. J. H. Clercx, and G. J. F. van Heijst, Phys. Fluids **13**, 1932 (2001).

[27] R. J. Lingwood and T. Alboussiere, Phys. Fluids **11**, 2058 (1999).

[28] P. G. Drazin, *Hydrodynamic Stability* (Cambridge University Press, Cambridge, 1981).

[29] L. D. Landau and E. M. Lifshitz, *Fluid Mechanics* (Pergamon Press, Oxford, 1959).

[30] P. Bergé, Y. Pomeau, C. Vidal, and D. Ruelle, *Order Within Chaos: Towards a Deterministic Approach to Turbulence* (Wiley, New York, 1984).